https://doi.org/10.5194/egusphere-2025-147
Preprint. Discussion started: 25 February 2025

Efficient use of a Lagrangian Particle Dispersion Model for atmospheric inversions using satellite observations of column mixing ratios

Rona L. Thompson[1], Nalini Krishnankutty[1], Ignacio Pisso[1], Philipp Schneider[1], Kerstin Stebel[1], Motoki Sasakawa[2], Andreas Stohl[3] and Stephen Platt[1]

[1]NILU, Kjeller, Norway
[2]Earth System Division, National Institute for Environmental Studies, Tsukuba, Japan
[3]University of Vienna, Vienna, Austria

Correspondence to: Rona L. Thompson (rlt@nilu.no)

Abstract

Satellite instruments for measuring atmospheric column mixing ratios have improved significantly over the past couple of decades with increases in pixel resolution and accuracy. As a result, satellite observations are being increasingly used in atmospheric inversions to improve estimates of emissions of greenhouse gases (GHGs), particularly CO_2 and CH_4, and to constrain regional and national emission budgets. However, in order to make use of the increasing resolution in inversions, the atmospheric transport models used need to be able to represent the observations at these finer resolutions. Here, we present a new and computationally efficient methodology to model satellite column average mixing ratios with a Lagrangian Particle Dispersion Model (LPDM) and calculate the Jacobian matrices describing the relationship between surface fluxes of GHGs and atmospheric column average mixing ratios, as needed in inversions. We present a case study using this methodology in the LMPD, FLEXPART, and the inversion framework, FLEXINVERT, to estimate CH_4 fluxes over Siberia using column average mixing ratios of CH_4 (XCH_4) from the TROPOMI instrument onboard the Sentinel-5P satellite. The results of the inversion using TROPOMI XCH_4 are evaluated against results using ground-based observations.

1. Introduction

Satellite remote sensing provides a wealth of information on the atmosphere and its composition. The number of satellite missions monitoring long-lived greenhouse gases (GHGs), specifically CO_2 and CH_4, has grown substantially over the past couple of decades providing information on their variability, trends, and sources. From instruments onboard satellites it is possible to retrieve mixing ratios of GHGs, most commonly as column averages (e.g. XCO_2 and XCH_4) or, depending on the instrument, viewing angle and retrieval, as sub-columns, which can be used to derive estimates of surface-atmosphere fluxes using atmospheric transport models and inversion techniques (e.g. Alexe et al., 2015; Chen et al., 2023; Chevallier et al., 2005; Peiro et al., 2022; Zhang et al., 2023, 2021). Satellite instruments can be classified as "area flux mappers" or "point source

https://doi.org/10.5194/egusphere-2025-147
Preprint. Discussion started: 25 February 2025

imagers" (Jacob et al., 2022). Area flux mappers are high precision instruments with larger pixel sizes (order of 0.1 to 10 km) and are designed to image mixing ratios on regional to global scales while point source imagers have smaller pixel size (< 0.1 km) and are designed to detect and quantify individual sources by mapping their plumes (Jacob et al., 2022). Specifically, it is the area flux mappers that are useful in inversions to estimate global and regional fluxes of CO_2 and CH_4, and they are becoming increasingly used to determine regional and national emission budgets and for comparisons with GHG emission inventories (e.g. Byrne et al., 2023; Deng et al., 2022; Maasakkers et al., 2021; Nesser et al., 2023; Worden et al., 2022). As satellite instrumentation has improved, there has also been an increase in pixel resolution. For example, for CH_4 the earliest satellite observations were from the SCIAMACHY instrument onboard ENVISAT, launched in 2002, which had a pixel size of 30 × 60 km, while the XCH_4 product from TROPOMI (TROPOspheric Monitoring Instrument) onboard Sentinel-5P, launched in 2017, has a pixel size at nadir of 5.5 × 7 km, and the recently launched MethaneSAT has a pixel size of just 0.1 × 0.4 km (Jacob et al., 2022). With this resolution increase it is important to consider how the observations are represented in atmospheric transport models for inverse modelling.

Up to the present, inversions with satellite observations have primarily been made using Eulerian atmospheric transport models, either using Green's functions, adjoint models or ensemble approaches to relate the column average mixing ratios to fluxes (e.g. Bergamaschi et al., 2009; Tsuruta et al., 2023; Varon et al., 2023). This is because the number of model iterations or ensemble members is independent of the number of observations, which for satellites can be a very large number. In contrast, Lagrangian particle dispersion models (LPDMs) have not been used to any significant extent with satellite observations, because the number of model calculations required in their backwards mode is proportional to the number of observations making it computationally demanding.

On the other hand, LPDMs have some advantages over Eulerian models. LPDMs exhibit less numerical diffusion compared to Eulerian models, and because of this, generally better capture tracer filaments generated by atmospheric dispersion (Ottino, 1989) and fine structures in tracers mixing ratios resulting from long-range transport (Rastigejev, 2010). Furthermore, LPDMs can accurately represent any observation geometry, whereas in Eulerian models an observation is represented by a grid cell (Pisso, 2019). With the increasing resolution of satellite instruments, Eulerian model resolution may become a limiting factor in the ability to accurately represent an observation, hence the use of LPDMs becomes a more interesting alternative. Finally, LPDMs can be run in a backwards in time mode (without significant modifications to the code and computational cost), which allows the sensitivity of an observation to fluxes to be calculated, and in this way LPDMs are sometimes said to be "self adjoint".

The main challenge of using LPDMs with satellite observations is the number of observations for which backwards computations need to be made, and that each retrieval is made over numerous vertical layers, which need to be represented in the model and combined with the retrieval's averaging kernel and prior mixing ratio profile. Here, we present a methodology

https://doi.org/10.5194/egusphere-2025-147
Preprint. Discussion started: 25 February 2025

for representing total column observations efficiently in an LPDM and open the possibility to use LPDMs across a variety of spatial and temporal scales for atmospheric inversions with satellite data. The methodology has been implemented in the LPDM, FLEXPART (FLEXible PARTicle dispersion model, version 10.4), but could be in principle be implemented in any LPDM. It can also be applied to any satellite retrieval.

We demonstrate the use of FLEXPART in a case study looking at CH_4 using retrievals from TROPOMI on board the Sentinel-5P satellite. The case study region is Siberia, which was chosen because it has significant CH_4 emissions from both natural sources (e.g. peatlands) and anthropogenic sources (e.g., fugitive emissions from oil and gas extraction and transportation as well as from coal mining). We use FLEXPART to model XCH_4 and, along with observed XCH_4, we derive estimates of CH_4 fluxes using the Bayesian inversion framework, FLEXINVERT (Thompson and Stohl, 2014). The fluxes from inversions using TROPOMI XCH_4 are evaluated by comparing with fluxes derived from inversions using ground-based in-situ observations from the JR-STATION network (Sasakawa et al., 2010, 2012).

2. Methodology

FLEXPART models atmospheric transport using virtual particles that are subject to transport and turbulent mixing as determined from meteorological fields. FLEXPART can be run in a backwards in time mode, which is theoretically consistent with the forward time mode calculations (Flesch et al., 1995; Thomson, 1990), to calculate the residence time of virtual particles in a surface layer within the boundary layer and thus the influence of surface fluxes on these particles. In this mode, Jacobian matrices representing the influence of fluxes on an atmospheric observation can be derived, which are termed "source-receptor-relationships" (SRRs), or sometimes "footprints" (Seibert and Frank, 2004). The SRRs can be integrated with flux fields to simulate mixing ratios and can be used in atmospheric inversions to update a prior estimate of the fluxes (e.g. Thompson and Stohl, 2014; Brioude et al., 2012). However, until now SRRs have only been calculated for point observations of atmospheric mixing ratios, and not for column average mixing ratios as observed by satellites.

2.1 Modelling total column observations with FLEXPART

Following Rodgers and Connor (2003) a modelled vertical profile, x of mixing ratios can be compared with a retrieved profile using:

$$x^{sm} = x^{pri} + \mathrm{A}(x - x^{pri}) \quad (1)$$

where A is the averaging kernel matrix (an $N \times N$ dimensional matrix), x^{pri} is the a priori profile used in the retrieval and x^{sm} is a smoothed version of the vertical profile, x. For a retrieval performed on N discrete pressure layers, the column average mixing ratio, x^{avg} is the weighted sum of N sub-columns corresponding to the retrieval pressure layers (Apituley et al., 2021):

$$x^{avg} = x^{avg,pri} + \sum_{n=1}^{N} a_n w_n x_n - \sum_{n=1}^{N} a_n w_n x_n^{pri} \quad (2)$$

https://doi.org/10.5194/egusphere-2025-147
Preprint. Discussion started: 25 February 2025

where $x^{avg,pri}$ is the prior column average mixing ratio, a_n is the nth element of the column averaging kernel, w_n is a pressure weighting term related to the thickness of the pressure layer, and x_n is the modelled mixing ratio for the nth retrieval layer. For LPDMs, x_n can be modelled as the product of the SRR for the nth retrieval layer, H_n, and the estimate of the fluxes, f, plus an estimate of the so-called "background" mixing ratio. Following Thompson and Stohl (2014), the background mixing ratio is modelled as the product of the background-receptor-relationship (BRR) matrix calculated from the positions of the virtual particles when they terminate, H_n^{ini} and a 3D field of initial mixing ratios, y^{ini}. Note, that chemical losses during the backward simulation period, e.g., from OH oxidation, can be taken into account in the SRR and BRR matrices. The modelled mixing ratio for the nth retrieval layer is thus:

$$x_n = \mathrm{H}_n f + \mathrm{H}_n^{ini} y^{ini} \quad (3)$$

By substituting Eq. 3 into Eq. 2 we obtain:

$$x^{avg} = x^{avg,pri} + \sum_{n=1}^{N} a_n (\mathrm{H}_n f w_n + \mathrm{H}_n^{ini} y^{ini} w_n) - \sum_{n=1}^{N} a_n w_n x_n^{pri} \quad (4)$$

Thus, the column average SRR can be expressed as:

$$\mathrm{H}^{col} = \sum_{n=1}^{N} a_n \mathrm{H}_n w_n \quad (5)$$

and similarly for the column average BRR, $H^{col,ini}$.

In FLEXPART, SRRs are calculated by sampling the particles on a regular three-dimensional grid. For a grid cell, ijk, the column SRR can be obtained as:

$$\mathrm{H}_{ijk}^{col} = \sum_{n=1}^{N} a_n w_n \frac{t}{m_n \rho_{ijk}} \sum_{p=1}^{J_{ijk,n}} m_p \quad (6)$$

where m_n is the total mass released for each retrieval layer, ρ_{ijk} is the air density in the grid cell, t is the sampling time, m_p is the mass of the individual particles (which can change in the case of atmospheric chemistry), and $J_{ijk,n}$ is the number of particles in the grid cell ijk originating from retrieval layer n. (Note, in Eq. 6 the nth element is equivalent to $a_n H_n w_n$). However, using Eq. 6 would still require maintaining information about which retrieval layer a particle had originated from in order to calculate the column SRR. Therefore, we carry the information of $a_n w_n$ in the mass released for each retrieval layer by varying the particle density, where the number of particles released per layer, P_n, is:

$$P_n = P a_n w_n \quad (7)$$

where P is the total number of particles released per retrieval. By rearranging Eq. 6 and substituting $a_n w_n$ for P_n/P we derive:

$$H_{ijk}^{col} = \frac{t}{m \rho_{ijk}} \sum_{n=1}^{N} \sum_{p=1}^{J_{ijk,n}} \frac{P_n}{P} m_p \quad (8)$$

Equation 8 can be further simplified to:

$$H_{ijk}^{col} = \frac{t}{m \rho_{ijk}} \sum_{p=1}^{J_{ijk}} m_p \quad (9)$$

in which the information on the retrieval layer a particle originated from does not need to be kept and is analogous to the calculation for point observations. This implementation was compared to calculating the SRRs for each layer individually, and

https://doi.org/10.5194/egusphere-2025-147
Preprint. Discussion started: 25 February 2025

the results were the same within the limits of numerical rounding errors. However, by implementing the calculation this way, total column observations can be simulated with the same computational cost as for point observations.

Similarly, the total column BRR for the grid cell *ijk* can be obtained as:

$$H_{ijk}^{col,ini} = \frac{1}{m}\sum_{n=1}^{N}\sum_{p=1}^{J_{ijk,n}}\frac{P_n}{P}m_p \quad (10)$$

A further consideration when modelling satellite observations with a Lagrangian model, is the geometry of the retrieval, since the ground-based pixels are not necessarily rectangular and can be rotated with respect to the meridians and parallels. In FLEXPART, an observation can be represented by releasing virtual particles from a volume in which the particles are distributed randomly. However, the default is that this volume is aligned with the meridians and parallels. Therefore, we have implemented an affine transformation on the particle positions so that the volume they represent matches the geometry of the retrieval.

2.2 Averaging of retrievals

Even with the efficient modelling of total column measurements using FLEXPART, current satellite missions can provide on the order of 10,000 to 100,000 retrievals globally per day, making the cost of computing backward trajectories for each retrieval still computationally expensive if the study region is large. For this reason, we average the retrievals to so-called "super observations". Averaging retrievals also has the advantage that the random error of the "super observation" is reduced compared to each individual retrieval.

However, in some areas where there is strong heterogeneity in the column average measurements, for instance, due to large localized sources, it would be advantageous to keep higher resolution observations. Therefore, we developed an optimal averaging routine in which the degree of averaging is based on the standard deviation of the column average mixing ratios. The user decides the finest resolution to be used, d_{min}, and the number of resolution steps, *nsteps*. The averaging is first performed for the coarsest resolution (given as $d_{min} \times 2^{nsteps-1}$), then the averaging is refined stepwise (from *nsteps*–1 to 0) by dividing grid cells where the standard deviation (recalculated at each step) is above a given threshold. Retrievals which are outside ±2 standard deviations of the mean are not included in the average. The averaging is redefined each day based on the available retrievals.

In the algorithm, the column average mixing ratio corresponding to the average of *M* retrievals is calculated as:

$$\bar{x} = \frac{1}{S}\sum_{m=1}^{M}\left(s_m x_m^{pri} + \sum_{n=1}^{N} s_m a_{mn} w_{mn}\left(x_{mn} - x_{mn}^{pri}\right)\right) \quad (11)$$

where $\bar{x}$ is the total column mixing ratio corresponding to the average, x_m^{pri} is the prior column average mixing ratio of the *m*th retrieval, *N* is the number of vertical layers in the retrievals, s_m is the surface area, and *S* is the total surface area of all retrievals. By rearranging Eq. 11 we obtain:

https://doi.org/10.5194/egusphere-2025-147
Preprint. Discussion started: 25 February 2025

$$\bar{x} = \frac{1}{S}\sum_{m=1}^{M} s_m x_m^{pri} + \frac{1}{S}\sum_{m=1}^{M}\sum_{n=1}^{N} s_m a_{mn} w_{mn} x_{mn} - \frac{1}{M}\sum_{m=1}^{M}\sum_{n=1}^{N} s_m a_{mn} w_{mn} x_{mn}^{pri} \quad (12)$$

and this can be written as:

$$\bar{x} = \overline{x^{pri}} + \sum_{n=1}^{N} \overline{a_n}\,\overline{w_n x_n} - \frac{1}{S}\sum_{m=1}^{M}\sum_{n=1}^{N} s_m a_{mn} w_{mn} x_{mn}^{pri} \qquad (if\ all\ x_{mn} = \overline{x_n}) \quad (13)$$

where $\overline{x^{pri}}$ is the area-weighted-average prior column mixing ratio, and $\overline{a_n}$, $\overline{w_n}$, $\overline{x_n}$ are the area-weighted-average column averaging kernel, pressure weighting, and mixing ratio corresponding to the *n*th layer. Note that the condition *if all* $x_{mn} = \overline{x_n}$ is met when the FLEXPART release is made for the area over which the *M* retrievals are averaged. The uncertainty of the super observation is calculated as the quadratic sum of the uncertainties of the individual retrievals weighted by the ground-pixel area of the retrievals.

3. Case study on methane sources in Siberia

We demonstrate the use of FLEXPART for modelling column average mixing ratios, as well as the averaging algorithm, in a case study looking at CH_4 emissions in Siberia. Siberia was chosen as it is a region with significant CH_4 emissions from both natural sources (e.g. peatlands) and anthropogenic sources (e.g., fugitive emissions from oil and gas extraction and transportation as well as from coal mining). It was also in Siberia that one of the largest point source emissions of CH_4 was detected by GHGSat – from a coal mine in the Kemerovo region (https://www.bbc.com/news/science-environment-61811481) and significant CH_4 sources have also been detected in this region by TROPOMI (Trenchev et al., 2023). On the other hand, Siberia is a challenging region to study, since there are no observations available north of around 50°N in the winter and the region is often cloudy, further limiting the number of available retrievals. Our inversion domain covers western and central Siberia (50° to 115°E and 40° to 80°N) and includes the Western Siberian Lowlands and major oil and gas fields, as well as important coal mining regions such as Kemerovo (Fig. 1). We limit the period of our study to March to October – months during which there are observations also north of 50°N and focus on the year 2020.

To evaluate the inversions using TROPOMI XCH_4, we make use of the JR-STATION ground-based network of CH_4 measurements. JR-STATION consists of 9 sites with in-situ measurements of CH_4 with the first sites having data from 2004 (Sasakawa et al., 2010, 2012).

3.1. Case study methodology

3.1.1 Inversion method

For the inversion we use the FLEXINVERT Bayesian inversion framework as described by Thompson and Stohl (2014). In this framework, the optimal fluxes are those that minimise the cost function:

$$J(z) = \frac{1}{2}(z - z_b)^{\mathrm{T}}\mathrm{B}^{-1}(z - z_b) + \frac{1}{2}(\mathrm{H}z - y)^{\mathrm{T}}\mathrm{R}^{-1}(\mathrm{H}z - y) \quad (14)$$

https://doi.org/10.5194/egusphere-2025-147
Preprint. Discussion started: 25 February 2025

where B is the prior error covariance matrix and describes the error and error correlation of the prior fluxes, R is the observation error covariance matrix and describes the uncertainty in the observations, z_b is the prior state vector, z is the optimal (or posterior) state vector, and y is the observation vector. The minimum of the cost function is found using the Lanczos version of the conjugate gradient algorithm (Lanczos, 1950). Although the Lanczos algorithm provides the Eigenvalues of the Hessian matrix $\nabla^2 J(z)$, in practice the number of iterations required to reach an accurate estimate of the posterior error covariance matrix is large. Therefore, the posterior uncertainty was calculated instead using a Monte Carlo ensemble following Chevallier et al. (2007).

The state vector variables include offsets to the prior fluxes, which are resolved at 14-day temporal resolution and at varying spatial resolution from 0.5° to 2.0° depending on how strongly the fluxes influence the observations (Thompson and Stohl, 2014). Only fluxes over land were optimized. This results in 2619 flux variables for each 14-day interval. The state vector also includes scalars of the boundary conditions (i.e., the initial mixing ratios in 3D space represented by the vector, y^{ini} in Eq. 3). The scalars are defined for four latitudinal bands, 90°-30°N, 30°N-0°, 0°-30°S, and 30°-90°S, and for three vertical layers, from 0-2000, 2000-10,000 and 10,000-70,000 metres above ground level, and are optimized for 28-day averages.

For the case study, FLEXPART was run using the ECMWF meteorological reanalysis data ERA5 at 0.5° and hourly resolution. Backwards trajectories were made using 30,000 particles for each TROPOMI super-observation. The trajectories were calculated for 20 days backwards in time from the time of the observation. The SRRs were calculated at 0.5° over the inversion domain and at 2.0° globally. In addition, the BRR (H_n^{ini} in Eq. 3) was calculated at the termination of the particles. For comparison with the inversions using TROPOMI retrievals, we also performed inversions using ground-based observations. The FLEXPART runs for these observations used the same set-up as for the retrievals but with only 20,000 particles per observation, which was deemed sufficient to represent a point observation.

The so-called background mixing ratio for each column average observation, was calculated as $H^{col,ini}y^{ini}$ (see Eq. 3-5) where y^{ini} is a 3D field of CH_4 mixing ratios (resolved daily) and was taken from the CAMS data assimilation product, EGG4 (https://ads.atmosphere.copernicus.eu/datasets/cams-global-ghg-reanalysis-egg4?tab=overview). In addition, we have used 3D mixing ratio fields from the CAMS Greenhouse gas inversion product TM5-4DVAR (https://atmosphere.copernicus.eu/greenhouse-gases-supplementary-products) in a sensitivity test.

3.1.2 Observations

In this case study, we use the Weighting Function Modified Differential Optical Absorption Spectroscopy (WFMD) retrieval product (version 1.8) from the University of Bremen (Schneising et al., 2019, 2023). We selected retrievals that had a quality flag of 0 (where the quality value ranges from good (0) to bad (1)). The retrievals were averaged to super observations, as described in Sect. 2.2, using two resolution steps with grid cell sizes of 0.25° and 0.5°. Uncertainties for the super observations

https://doi.org/10.5194/egusphere-2025-147
Preprint. Discussion started: 25 February 2025

were calculated as the quadratic sum of the uncertainty for each retrieval weighted by the area of the ground-pixel of the retrieval. The full observation-space uncertainty was the quadratic sum of the super-observation uncertainty and an uncertainty estimated for the background column average mixing ratio. The resulting observation space uncertainties were typically in the range of 14 to 20 ppb and the square of these were used as the variances in the observation error covariance matrix, and we assumed that errors in the super observations were uncorrelated. On average, there were 3781 super-observations per day.

For validation, we used ground-based observations from the Japan-Russia Siberian Tall Tower Inland Observation Network (JR-STATION) network (Sasakawa et al., 2010, 2012) (Fig. 1 and Table 1). It is comprised of nine (currently six operating) tower sites in Siberia where simultaneous multi-point semi-continuous observations of CO_2 and CH_4 have been made. The CH_4 mixing ratios were measured using a modified SnO_2 semiconductor sensor and determined against the NIES 94 CH_4 scale. The NIES 94 CH_4 scale ranges approximately 5 ppb higher than the WMO-CH4-X2004A scale. Thus, we adjusted the CH_4 mixing ratios to the WMO scale for use in the inversions. In addition, we used observations from the flask sampling sites Ulaan Uul, Mongolia (UUM) and Teriberka, Russia (TER), and in-situ observations from the Global Atmospheric Watch site, Cholpon-Ata, Kyrgyzstan (CPA).

3.1.3 Prior information

In the case study inversion, we optimize the total net CH_4 flux. A prior estimate for the total net flux was prepared using the following input datasets: i) the EDGAR-v8 for anthropogenic emissions (Crippa et al., 2023), ii) the land-surface model, LPX-Bern for natural fluxes from peatlands, wet and inundated soils, and the soil sink, iii) Etiope et al. (2019) for geological emissions, iv) GFED-v4.1s for biomass burning emissions (Werf et al., 2017), and v) the observation-based climatology of Weber et al. (2019) for ocean fluxes. An overview of the flux estimates used in the prior is given in Table 2. The input data are given at different temporal and spatial resolutions and thus were averaged/interpolated to the same spatial resolution as the SRRs for the inversion domain, i.e., 0.5° and interpolated to 14 days to match the state vector temporal resolution.

Prior uncertainties were calculated for each grid cell as 50% of the prior estimate but with a lower limit of 1×10^{-9} kg m^{-2} h^{-1}, which is approximately the 10^{th} percentile value of all fluxes over the inversion domain. The prior error covariance matrix, B, was calculated using the square of the prior uncertainties in each grid cell as the variances and the co-variances were calculated assuming that the correlation between two grid cells decays exponentially with a correlation scale length of 200 km.

3.2 Results and discussion

3.2.1 Modelled XCH_4

Column mixing ratios of CH_4 were modelled for each of the super-observations using the set-up described above. The observations for all months show high XCH_4 values for the southern part of the domain, especially in northern China. This is

https://doi.org/10.5194/egusphere-2025-147
Preprint. Discussion started: 25 February 2025

also captured, but with lesser magnitude, in the prior and posterior modelled XCH_4 (Fig. 2). In the summer months (June to August) there is also elevated XCH_4 in the central part of the domain, corresponding to the location of wetlands but also to oil and gas fields. The posterior modelled XCH_4 had a much closer agreement with the observations, as expected. For example, for March the a posteriori Mean Error (ME) and Root Mean Square Error (RMSE) was 2 and 16 ppb, compared to that a priori with 45 and 50 ppb, respectively. For July, the a posteriori ME and RMSE was 3 and 13 ppb, compared to that a priori with 12 and 20 ppb.

The generally too high modelled XCH_4 using the prior state vector, especially in March, was primarily due to a too high background estimate when this was based on initial mixing ratios from EGG4. Further simulations using the CAMS greenhouse gas inversion product (CAMSv20r1) showed that the modelled XCH_4 is strongly sensitive to the fields of initial mixing ratio used, and using CAMSv20r1 the prior modelled XCH_4 was considerably lower (see Supplementary Fig. S1). The reason is the different vertical distributions of CH_4 in CAMSv20r1 versus EGG4 (see Supplementary Fig. S2), which convolved with the averaging kernel and the FLEXPART-calculated averaging matrix, $H^{ini,col}$ lead to quite different values for the background column average mixing ratio. A bias is also seen when XCH_4 is calculated directly from the initial mixing ratio fields (by applying Eq. 2) with EGG4 resulting in significantly higher, and CAMSv20r1 resulting in significantly lower, XCH_4 compared to the observations in March, but with smaller biases in July (see Supplementary Fig. S3). For this reason, the boundary conditions (i.e., 3D fields of initial mixing ratios) are optimized in the inversion simultaneously with the fluxes.

In the inversion using EGG4, the posterior scalars of initial mixing ratios were decreased in the latitude band 30°-90°N at all altitude layers and timesteps, while the mixing ratios in the band 0°-30°N were increased slightly in the lowest altitude layer and more strongly in the upper two layers, while the scalars for the Southern Hemisphere did not differ significantly from the prior value of 1.0 (Fig. 3). In contrast, in the inversion using CAMSv20r1, the scalars for 30-90°N were decreased only for the lowest altitude layer, remained close to the prior value for the mid layer and increased for the uppermost layer (see Supplementary Fig. S4). Despite the very different background estimates using EGG4 versus CAMSv20r1, the inversions resulted in very similar posterior fluxes, which indicates that the optimization of the boundary conditions is successful in minimizing biases due to these (see Supplementary Fig. S5).

Figure 4 shows the area-weighted mean XCH_4 for the domain for 2-weekly intervals from March to October. The prior modelled XCH_4 follows the prior background estimate, which is driven by variations in the boundary conditions (based on EGG4) and differs considerably from the variation in the observed XCH_4. After optimization, the modelled XCH_4 more closely follows the observations, which is largely due to the improvement to the background estimate. Both the prior and posterior modelled XCH_4 remain close to their respective backgrounds until late April, when fluxes in the domain start to increase and thus have a more significant impact on XCH_4 and return towards their background estimate after September.

https://doi.org/10.5194/egusphere-2025-147
Preprint. Discussion started: 25 February 2025

3.2.2 Posterior fluxes and uncertainty reduction using TROPOMI

Figure 5 shows the mean posterior fluxes estimated from the inversion using TROPOMI observations as well as the posterior minus prior differences (flux increments). Overall, the posterior fluxes remain very close to those of the prior and the total mean posterior source over the domain for March to October is 30.3 Tg/y compared to the prior estimate of 31.0 Tg/y. The seasonal cycle also remained close to the prior estimate with a maximum in late July to early August (Fig. 6). The inversion did, however, reduce emissions for a few hotspots in northwestern Siberia in grid cells with important oil and gas sources, and increase emissions for a few hotspots in northern China, again in grid cells with important oil and gas sources.

It must be noted, however, that the uncertainty reduction on the fluxes (calculated as one minus the ratio of the posterior to prior flux uncertainty) is quite small and mainly limited to the areas of the Western Siberian Lowlands and to the southern part of the domain, where it reaches 20-50% (Fig. 7). This is similar to the results of Tsuruta et al. (2023), who likewise found limited uncertainty reduction for the high northern latitudes using TROPOMI and little difference between the prior and posterior fluxes for their region of Eurasia (including Fennoscandia). This is at least in part due to the poor observational coverage over Siberia where even outside of the winter season the number of observations is still limited due to frequent cloud cover (Gao et al., 2023). The pattern of uncertainty reduction in our study is persistent for all months and is largely determined by the distribution of observations and of the prior flux uncertainty. The more southern part of the domain is better covered by observations, especially over Kazakhstan and northern China, while the prior flux uncertainties followed the distribution of the prior fluxes with larger uncertainties in the area of the Western Siberian Lowlands and for grid cells with hotspot emissions (see Supplementary Fig. S6).

3.2.3 Comparison with ground-based data inversions

Figures 8a and 8b show the posterior fluxes and flux increments, respectively, from the inversion with ground-based observations. The mean posterior fluxes show large emissions over the Western Siberian Lowlands, and generally higher emissions than in the prior estimate. They also indicate that some of the hotspot emission sources in northwestern Siberia are too large in the prior, which is consistent with the result of the inversion using TROPOMI. Moreover, the posterior fluxes indicate larger emissions for a few hotspots in southern Siberia coinciding with grid cells where there are coal mines. The mean posterior source over the domain from March to October is 33.9 Tg y^{-1}. The difference between the posterior fluxes from the inversion using ground-based observations versus that using TROPOMI (Fig. 8c) follows a very similar pattern to the posterior minus prior flux increments (Fig. 8b), as expected, since the posterior fluxes from the inversion using TROPOMI are very close to the prior.

The ground-based observation inversion indicates an earlier and more intense summer maximum compared to the prior estimate and to the estimate from the TROPOMI based inversion (Fig. 6). In the ground-based inversion the maximum occurs

https://doi.org/10.5194/egusphere-2025-147
Preprint. Discussion started: 25 February 2025

in early July, versus late July to early August in the prior, and reaches a maximum of 49.4 Tg y^{-1} for the mean of July versus 37.8 Tg y^{-1} in the prior.

Moreover, the inversion using ground-based observations is better constrained than that using TROPOMI, and there are uncertainty reductions of up to 50% over a significant part of Western Siberia, corresponding to where the continuous measurement sites are located, although some gaps remain (Fig. 9). On the other hand, the southern and eastern parts of the domain are less well constrained.

As a further check on the inversion using TROPOMI observations, we compared the mixing ratios modelled using the prior fluxes, the posterior fluxes from the ground-based inversion, and the posterior fluxes from the TROPOMI inversion, against observations at all ground-based sites (Fig. 10). In this comparison, the optimized boundary conditions were used to show only the differences due to the fluxes. Overall, there is an improvement in the fit to the observations using the posterior fluxes from the ground-based inversion compared to the prior fluxes as would be expected since these observations were used in the inversion. The RMSE over all observations was reduced from 37 ppb a priori to 25 ppb a posteriori. However, using the posterior fluxes from the inversion using TROPOMI observations, did not lead to an improvement (nor a deterioration) in the fit to the observations, which is simply because the posterior fluxes in this case remained very close to the prior.

4. Summary and conclusions

We have developed an efficient method to model total column observations, such as those from satellites, using a Lagrangian Particle Dispersion Model (LPDM) and, furthermore, to compute Jacobian matrices describing the relationship between fluxes and the change in the column average mixing ratio as needed in inverse modelling. This method means that the computations are in principle no more costly than those for point observations. However, since backwards calculations are still needed for each observation, the computational cost is still a limiting factor for using this method on the global scale for satellites providing a very large number of retrievals, e.g. TROPOMI which provides ~100,000 retrievals globally each day. This limitation can be overcome though by using "super observations", that is averages of retrievals, which reduces the number of calculations required. On the other hand, our method using an LPDM is well suited for regional inversion studies especially with observations from flux mapping satellites with a relatively high resolution, such as the TROPOMI XCH_4 product with a resolution of 5.5 × 7 km, the recently launched MethaneSAT with a resolution of 0.1 × 0.4 km, and the future missions, CO2M with 2 × 2 km and GeoCarb with 6 × 3 km.

We presented a case study using the methodology to estimate CH_4 fluxes over Siberia using WFMD retrievals of XCH_4 from the TROPOMI instrument. We found that, for this northern region, the boundary conditions have a strong influence on the modelled column mixing ratios, but by optimizing the boundary conditions any bias in these does not contribute to a bias in the posterior fluxes. Moreover, we compared the inversion with TROPOMI to one using ground-based observations. The

https://doi.org/10.5194/egusphere-2025-147
Preprint. Discussion started: 25 February 2025

ground-based observations provide a stronger constraint on the fluxes and greater uncertainty reduction compared to TROPOMI for this northern region. Although the posterior fluxes obtained using TROPOMI remained close to the prior, there were some consistent results with those obtained using ground-based observations, namely, a decrease in hotspot emissions in northern Siberia and an increase in a hotspot emission in northern China compared to the prior emissions.

Based on these results, the caveats of using satellite retrievals in regional inversions at high latitudes are: 1) the strong dependence of the modelled column mixing ratios on the boundary conditions and hence the need to set large uncertainties for the optimization of the boundary conditions, which has the effect of reducing the constraint of the observed column average mixing ratios on the fluxes, and 2) the limited observational coverage and constraint of the column average mixing ratios on surface fluxes in Siberia and hence low uncertainty reduction from inversions.

Author contribution

RLT designed the algorithms, wrote the code, ran the ground-based observation inversions and wrote the manuscript. NK ran FLEXPART for the satellite retrievals, ran the satellite-based inversions, and contributed to the manuscript. PS, IP, KS, SP, AS and MS provided advice on the use of the satellite data and modelling with FLEXPART and contributed to the manuscript.

Competing interest statement

The authors declare that they have no conflict of interest.

Data availability

TROPOMI WFMD retrieval data as well as the corresponding data documentation are available from the University of Bremen at https://www.iup.uni-bremen.de/carbon_ghg/products/tropomi_wfmd/. The JR-STATION data are available from the Global Environmental Database, hosted by ESD, NIES: http://db.cger.nies.go.jp/portal/geds/index. The FLEXINVERT and FLEXPART codes used for this study are available from the GitLab repository: https://git.nilu.no/flexpart.

Acknowledgements

This study was supported by the ReGAME project funded by the Research Council of Norway (grant no. 325610) and by the Horizon Europe project, EYE-CLIMA (grant no. 101081395). AS was partly supported by the Austrian Research Promotion Agency under the project GHG-KIT (ID 42635422). We would like to acknowledge Oliver Schneising (University of Bremen) for providing the TROPOMI WFMD retrievals. Development of the TROPOMI WFMD product was supported by the European Space Agency via the projects GHG-CCI+, MethaneCAMP, and SMART-CH4 (ESA contract nos.

https://doi.org/10.5194/egusphere-2025-147
Preprint. Discussion started: 25 February 2025

4000126450/19/I-NB, 4000137895/22/I-AG, and 4000142730/23/I-NS) and the Bundesministerium für Bildung und Forschung within its project ITMS (grant no. 01 LK2103A).

https://doi.org/10.5194/egusphere-2025-147
Preprint. Discussion started: 25 February 2025

References

Alexe, M., Bergamaschi, P., Segers, A., Detmers, R., Butz, A., Hasekamp, O., Guerlet, S., Parker, R., Boesch, H., and Frankenberg, C.: Inverse modelling of CH 4 emissions for 2010--2011 using different satellite retrieval products from GOSAT and SCIAMACHY, Atmos. Chem. Phys., 15, 113–133, https://doi.org/10.5194/acp-15-113-2015, 2015.

Apituley, A., Pedergnana, M., Sneep, M., Veefkind, J., Loyola, D., Hasekamp, O., Delgado, A. L., and Borsdorff, T.: Sentinel-5 precursor TROPOMI: Level 2 Product User Manual Methane, 2021.

Bergamaschi, P., Frankenberg, C., Meirink, J. F., Krol, M., Villani, M. G., Houweling, S., Dentener, F., Dlugokencky, E. J., Miller, J. B., Gatti, L. V., Engel, A., and Levin, I.: Inverse modeling of global and regional CH4 emissions using SCIAMACHY satellite retrievals, Journal of Geophysical Research: Atmospheres, 114, D22301, https://doi.org/10.1029/2009jd012287, 2009.

Brioude, J., Petron, G., Frost, G. J., Ahmadov, R., Angevine, W. M., Hsie, E. Y., Kim, S. W., Lee, S. H., McKeen, S. A., Trainer, M., Fehsenfeld, F. C., Holloway, J. S., Peischl, J., Ryerson, T. B., and Gurney, K. R.: A new inversion method to calculate emission inventories without a prior at mesoscale: Application to the anthropogenic CO2 emission from Houston, Texas, Journal of Geophysical Research-Atmospheres, 117, D05312, https://doi.org/10.1029/2011jd016918, 2012.

Byrne, B., Baker, D. F., Basu, S., Bertolacci, M., Bowman, K. W., Carroll, D., Chatterjee, A., Chevallier, F., Ciais, P., Cressie, N., Crisp, D., Crowell, S., Deng, F., Deng, Z., Deutscher, N. M., Dubey, M. K., Feng, S., García, O. E., Griffith, D. W. T., Herkommer, B., Hu, L., Jacobson, A. R., Janardanan, R., Jeong, S., Johnson, M. S., Jones, D. B. A., Kivi, R., Liu, J., Liu, Z., Maksyutov, S., Miller, J. B., Miller, S. M., Morino, I., Notholt, J., Oda, T., O'Dell, C. W., Oh, Y.-S., Ohyama, H., Patra, P. K., Peiro, H., Petri, C., Philip, S., Pollard, D. F., Poulter, B., Remaud, M., Schuh, A., Sha, M. K., Shiomi, K., Strong, K., Sweeney, C., Té, Y., Tian, H., Velazco, V. A., Vrekoussis, M., Warneke, T., Worden, J. R., Wunch, D., Yao, Y., Yun, J., Zammit-Mangion, A., and Zeng, N.: National CO2 budgets (2015–2020) inferred from atmospheric CO2 observations in support of the global stocktake, Earth Syst. Sci. Data, 15, 963–1004, https://doi.org/10.5194/essd-15-963-2023, 2023.

Chen, Z., Jacob, D. J., Gautam, R., Omara, M., Stavins, R. N., Stowe, R. C., Nesser, H., Sulprizio, M. P., Lorente, A., Varon, D. J., Lu, X., Shen, L., Qu, Z., Pendergrass, D. C., and Hancock, S.: Satellite quantification of methane emissions and oil–gas methane intensities from individual countries in the Middle East and North Africa: implications for climate action, Atmos. Chem. Phys., 23, 5945–5967, https://doi.org/10.5194/acp-23-5945-2023, 2023.

Chevallier, F., Fisher, M., Peylin, P., Serrar, S., Bousquet, P., Breon, F. M., Chédin, A., and Ciais, P.: Inferring CO2 sources and sinks from satellite observations: Method and application to TOVS data, Journal of Geophysical Research-Atmospheres, 110, https://doi.org/10.1029/2005jd006390, 2005.

Chevallier, F., Bréon, F.-M., and Rayner, P. J.: Contribution of the Orbiting Carbon Observatory to the estimation of CO2 sources and sinks: Theoretical study in a variational data assimilation framework, Journal of Geophysical Research-Atmospheres, 112, https://doi.org/10.1029/2006jd007375, 2007.

Crippa, M., Guizzardi, D., Banja, F., Banja, M., Muntean, M., Schaaf, E., Becker, W., Montforti-Ferrario, F., Quadrelli, R., Martin, A. R., Taghavi-Moharamli, P., Köykkä, J., Grassi, G., Rossi, S., Melo, J. B. D., Oom, D., Branco, A., San-Miguel, J., and Vignati, E.: GHG Emissions of all World Countries, Publications Office of the European Union, Luxembourg, 2023.

Deng, Z., Ciais, P., Tzompa-Sosa, Z. A., Saunois, M., Qiu, C., Tan, C., Sun, T., Ke, P., Cui, Y., Tanaka, K., Lin, X., Thompson, R. L., Tian, H., Yao, Y., Huang, Y., Lauerwald, R., Jain, A. K., Xu, X., Bastos, A., Sitch, S., Palmer, P. I., Lauvaux, T., d'Aspremont, A., Giron, C., Benoit, A., Poulter, B., Chang, J., Petrescu, A. M. R., Davis, S. J., Liu, Z., Grassi, G., Albergel, C., Tubiello, F. N., Perugini, L., Peters, W., and Chevallier, F.: Comparing national greenhouse gas budgets reported in UNFCCC inventories against atmospheric inversions, Earth Syst Sci Data, 14, 1639–1675, https://doi.org/10.5194/essd-14-1639-2022, 2022.

Etiope, G., Ciotoli, G., Schwietzke, S., and Schoell, M.: Gridded maps of geological methane emissions and their isotopic signature, Earth Sys Sci Data, 11, 1–22, https://doi.org/10.5194/essd-11-1-2019, 2019.

Flesch, T. K., Wilson, J. D., and Yee, E.: Backward-time Lagrangian stochastic dispersion models and their application to estimate gaseous emissions, Journal of Applied Meteorology, 34, 1320–1332, 1995.

Gao, M., Xing, Z., Vollrath, C., Hugenholtz, C. H., and Barchyn, T. E.: Global observational coverage of onshore oil and gas methane sources with TROPOMI, Sci. Rep., 13, 16759, https://doi.org/10.1038/s41598-023-41914-8, 2023.

Jacob, D. J., Varon, D. J., Cusworth, D. H., Dennison, P. E., Frankenberg, C., Gautam, R., Guanter, L., Kelley, J., McKeever, J., Ott, L. E., Poulter, B., Qu, Z., Thorpe, A. K., Worden, J. R., and Duren, R. M.: Quantifying methane emissions from the global scale down to point sources using satellite observations of atmospheric methane, Atmos. Chem. Phys., 22, 9617–9646, https://doi.org/10.5194/acp-22-9617-2022, 2022.

Lanczos, C.: An iteration method for the solution of the eigenvalue problem, J. Res. Natl. Bur. Standards, 45, 255–282, 1950.

Maasakkers, J. D., Jacob, D. J., Sulprizio, M. P., Scarpelli, T. R., Nesser, H., Sheng, J., Zhang, Y., Lu, X., Bloom, A. A., Bowman, K. W., Worden, J. R., and Parker, R. J.: 2010–2015 North American methane emissions, sectoral contributions, and trends: a high-resolution inversion of GOSAT observations of atmospheric methane, Atmos. Chem. Phys., 21, 4339–4356, https://doi.org/10.5194/acp-21-4339-2021, 2021.

Nesser, H., Jacob, D. J., Maasakkers, J. D., Lorente, A., Chen, Z., Lu, X., Shen, L., Qu, Z., Sulprizio, M. P., Winter, M., Ma, S., Bloom, A. A., Worden, J. R., Stavins, R. N., and Randles, C. A.: High-resolution U.S. methane emissions inferred from an inversion of 2019 TROPOMI satellite data: contributions from individual states, urban areas, and landfills, EGUsphere, 2023, 1–36, https://doi.org/10.5194/egusphere-2023-946, 2023.

Peiro, H., Crowell, S., and III, B. M.: Optimizing 4 years of CO2 biospheric fluxes from OCO-2 and in situ data in TM5: fire emissions from GFED and inferred from MOPITT CO data, Atmos. Chem. Phys., 22, 15817–15849, https://doi.org/10.5194/acp-22-15817-2022, 2022.

Rodgers, C. D. and Connor, B. J.: Intercomparison of remote sounding instruments, J Geophys Res Atmospheres, 108(D3), 4116, https://doi.org/10.1029/2002jd002299, 2003.

Sasakawa, M., Shimoyama, K., Machida, T., Tsuda, N., Suto, H., Arshinov, M., Davydov, D., Fofonov, A., Krasnov, O., and Saeki, T.: Continuous measurements of methane from a tower network over Siberia, Tellus B, 62, 403–416, https://doi.org/10.1111/j.1600-0889.2010.00494.x, 2010.

Sasakawa, M., Ito, A., Machida, T., Tsuda, N., Niwa, Y., Davydov, D., Fofonov, A., and Arshinov, M.: Annual variation of CH4 emissions from the middle taiga in West Siberian Lowland (2005–2009): a case of high CH4 flux and precipitation rate in the summer of 2007, Tellus, 64, 2012.

https://doi.org/10.5194/egusphere-2025-147
Preprint. Discussion started: 25 February 2025

Schneising, O., Buchwitz, M., Reuter, M., Bovensmann, H., Burrows, J. P., Borsdorff, T., Deutscher, N. M., Feist, D. G., Griffith, D. W. T., Hase, F., Hermans, C., Iraci, L. T., Kivi, R., Landgraf, J., Morino, I., Notholt, J., Petri, C., Pollard, D. F., Roche, S., Shiomi, K., Strong, K., Sussmann, R., Velazco, V. A., Warneke, T., and Wunch, D.: A scientific algorithm to simultaneously retrieve carbon monoxide and methane from TROPOMI onboard Sentinel-5 Precursor, Atmos. Meas. Tech., 12, 6771–6802, https://doi.org/10.5194/amt-12-6771-2019, 2019.

Schneising, O., Buchwitz, M., Hachmeister, J., Vanselow, S., Reuter, M., Buschmann, M., Bovensmann, H., and Burrows, J. P.: Advances in retrieving XCH4 and XCO from Sentinel-5 Precursor: improvements in the scientific TROPOMI/WFMD algorithm, Atmos. Meas. Tech., 16, 669–694, https://doi.org/10.5194/amt-16-669-2023, 2023.

Seibert, P. and Frank, A.: Source-receptor matrix calculation with a Lagrangian particle dispersion model in backward mode, Atmos. Chem. Phys, 4, 51–63, https://doi.org/10.5194/acp-4-51-2004, 2004.

Thompson, R. L. and Stohl, A.: FLEXINVERT: an atmospheric Bayesian inversion framework for determining surface fluxes of trace species using an optimized grid, Geosci Model Dev, 7, 2223–2242, https://doi.org/10.5194/gmd-7-2223-2014, 2014.

Thomson, D. J.: A stochastic model for the motion of particle pairs in isotropic high-Reynolds-number turbulence, and its application to the problem of concentration variance, Journal of Fluid Mechanics, 210, 113–153, https://doi.org/10.1017/s0022112090001239, 1990.

Trenchev, P., Dimitrova, M., and Avetisyan, D.: Huge CH4, NO2 and CO Emissions from Coal Mines in the Kuznetsk Basin (Russia) Detected by Sentinel-5P, Remote Sens., 15, 1590, https://doi.org/10.3390/rs15061590, 2023.

Tsuruta, A., Kivimäki, E., Lindqvist, H., Karppinen, T., Backman, L., Hakkarainen, J., Schneising, O., Buchwitz, M., Lan, X., Kivi, R., Chen, H., Buschmann, M., Herkommer, B., Notholt, J., Roehl, C., Té, Y., Wunch, D., Tamminen, J., and Aalto, T.: CH4 Fluxes Derived from Assimilation of TROPOMI XCH4 in CarbonTracker Europe-CH4: Evaluation of Seasonality and Spatial Distribution in the Northern High Latitudes, Remote Sens., 15, 1620, https://doi.org/10.3390/rs15061620, 2023.

Varon, D. J., Jacob, D. J., Hmiel, B., Gautam, R., Lyon, D. R., Omara, M., Sulprizio, M., Shen, L., Pendergrass, D., Nesser, H., Qu, Z., Barkley, Z. R., Miles, N. L., Richardson, S. J., Davis, K. J., Pandey, S., Lu, X., Lorente, A., Borsdorff, T., Maasakkers, J. D., and Aben, I.: Continuous weekly monitoring of methane emissions from the Permian Basin by inversion of TROPOMI satellite observations, Atmos. Chem. Phys., 2023, 7503-7620, https://doi.org/10.5194/acp-23-7503-2023, 2023.

Weber, T., Wiseman, N. A., and Kock, A.: Global ocean methane emissions dominated by shallow coastal waters, Nature communications, 10, 1–10, https://doi.org/10.1038/s41467-019-12541-7, 2019.

Werf, G. R. V. der, Randerson, J. T., Giglio, L., Leeuwen, T. T. van, Chen, Y., Rogers, B. M., Mu, M., Marle, M. J. E. van, Morton, D. C., Collatz, G. J., Yokelson, R. J., and Kasibhatla, P. S.: Global fire emissions estimates during 1997–2016, Earth Syst. Sci. Data, 9, 697–720, https://doi.org/10.5194/essd-9-697-2017, 2017.

Worden, J. R., Cusworth, D. H., Qu, Z., Yin, Y., Zhang, Y., Bloom, A. A., Ma, S., Byrne, B. K., Scarpelli, T., Maasakkers, J. D., Crisp, D., Duren, R., and Jacob, D. J.: The 2019 methane budget and uncertainties at 1∘ resolution and each country through Bayesian integration Of GOSAT total column methane data and a priori inventory estimates, Atmos. Chem. Phys., 22, 6811–6841, https://doi.org/10.5194/acp-22-6811-2022, 2022.

https://doi.org/10.5194/egusphere-2025-147
Preprint. Discussion started: 25 February 2025

Zhang, L., Jiang, F., He, W., Wu, M., Wang, J., Ju, W., Wang, H., Zhang, Y., Sitch, S., Walker, A. P., Yue, X., Feng, S., Jia, M., and Chen, J. M.: A Robust Estimate of Continental-Scale Terrestrial Carbon Sinks Using GOSAT XCO2 Retrievals, Geophys. Res. Lett., 50, https://doi.org/10.1029/2023gl102815, 2023.

Zhang, Y., Jacob, D. J., Lu, X., Maasakkers, J. D., Scarpelli, T. R., Sheng, J.-X., Shen, L., Qu, Z., Sulprizio, M. P., Chang, J., Bloom, A. A., Ma, S., Worden, J., Parker, R. J., and Boesch, H.: Attribution of the accelerating increase in atmospheric methane during 2010–2018 by inverse analysis of GOSAT observations, Atmos. Chem. Phys., 21, 3643–3666, https://doi.org/10.5194/acp-21-3643-2021, 2021.

https://doi.org/10.5194/egusphere-2025-147
Preprint. Discussion started: 25 February 2025

Table 1: Ground-based atmospheric observation sites

Station ID	Station name, country	Measurement type	Latitude (°N)	Longitude (°E)	Altitude (masl)	Network/Institute
UUM	Ulaan Uul, Mongolia	Flask	44.45	111.09	1007	NOAA
TER	Teriberka, Russia	Flask	69.20	35.10	40	Voeikov Main Geophysical Observatory
CPA	Cholpon-Ata, Kyrgyzstan	In-situ	42.64	77.07	1613	Agency on Hydrometeorology under Ministry of Emergency Situations of the Kyrgyz Republic
AZV	Azovo, Russia	In-situ	54.71	73.03	110	JRSTATION
BRZ	Berezorechka, Russia	In-situ	56.15	84.33	168	JRSTATION
DEM	Demyanskoe, Russia	In-situ	59.79	70.87	63	JRSTATION
KRS	Karasevoe, Russia	In-situ	58.25	82.42	76	JRSTATION
NOY	Noyabrsk, Russia	In-situ	63.43	75.78	108	JRSTATION
VGN	Vaganovo, Russia	In-situ	54.50	62.32	192	JRSTATION

Table 2: Overview of flux estimates used in the prior

Source type	Description	Resolution	Total for domain (Tg CH_4)
Anthropogenic	EDGAR-v8	0.1°, annual	12.8
Peatlands, wet and inundated soils, soil sink	LPX-Bern	0.5°, monthly	Peatlands: 11.5 Wet and inundated soils: 5.8 Soil sink: -2.8
Biomass burning	GFED-v4.1s	0.25°, monthly	1.2
Ocean	Weber et al. (2019)	0.25°, monthly	0.5
Geological	Etiope et al. (2019)	1.0°, annual	1.6

https://doi.org/10.5194/egusphere-2025-147
Preprint. Discussion started: 25 February 2025

Figure 1: Map of the inversion domain indicating oil &gas extraction and coal mining locations and the ground-based sites used in the inversion. The oil & gas and coal mining data were obtained from Global Energy Monitor (https://globalenergymonitor.org).

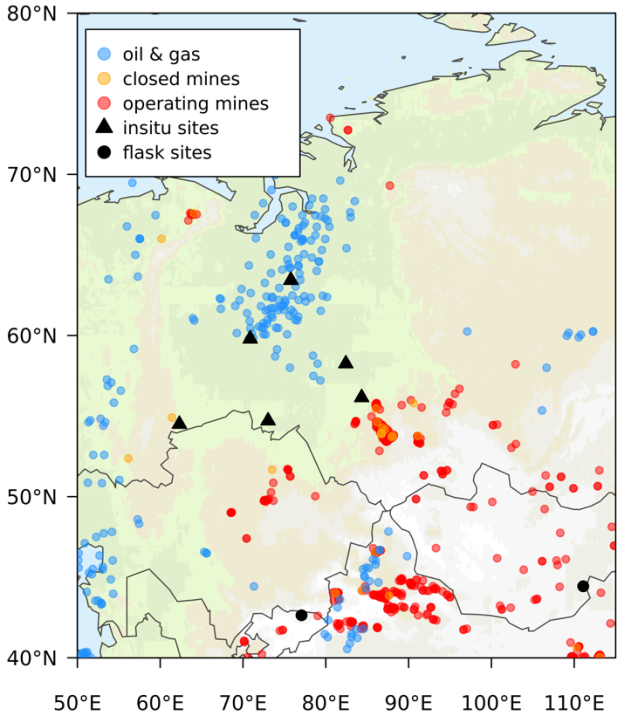

505

https://doi.org/10.5194/egusphere-2025-147
Preprint. Discussion started: 25 February 2025

Figure 2: Monthly mean XCH_4 in ppb for March 2020 from a) observations, b) modelled using prior fluxes, and c) modelled using posterior fluxes and scalars of initial mixing ratios. Panels d) to f) are as for a) to c) but for the monthly mean XCH_4 for July 2020.

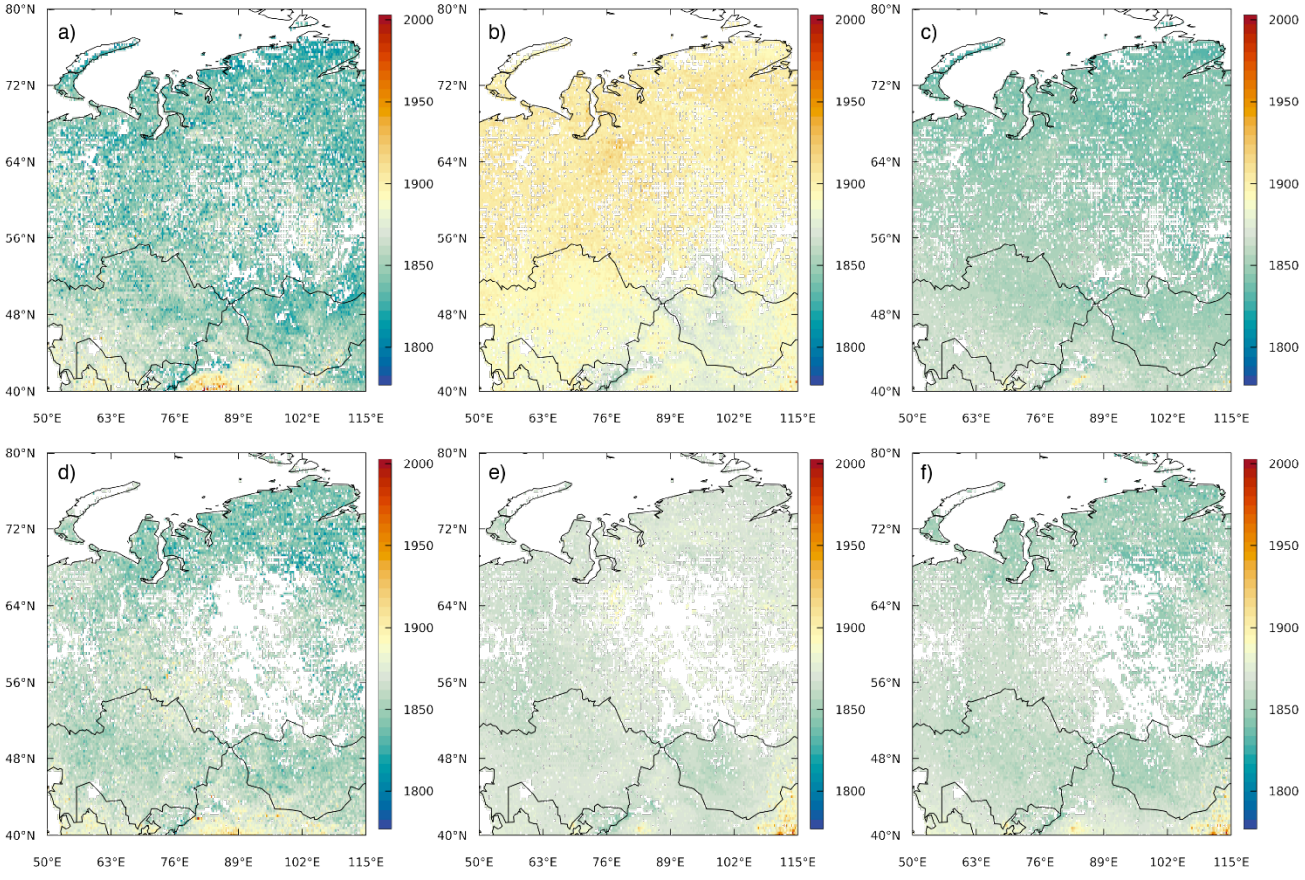

510

https://doi.org/10.5194/egusphere-2025-147
Preprint. Discussion started: 25 February 2025

Figure 3: Posterior scalars of the initial mixing ratios from the TROPOMI inversion using 3D initial mixing ratio fields from EGG4. In each sub-panel, the scalars are shown for each timestep of 28 days and for each of the four latitude bands.

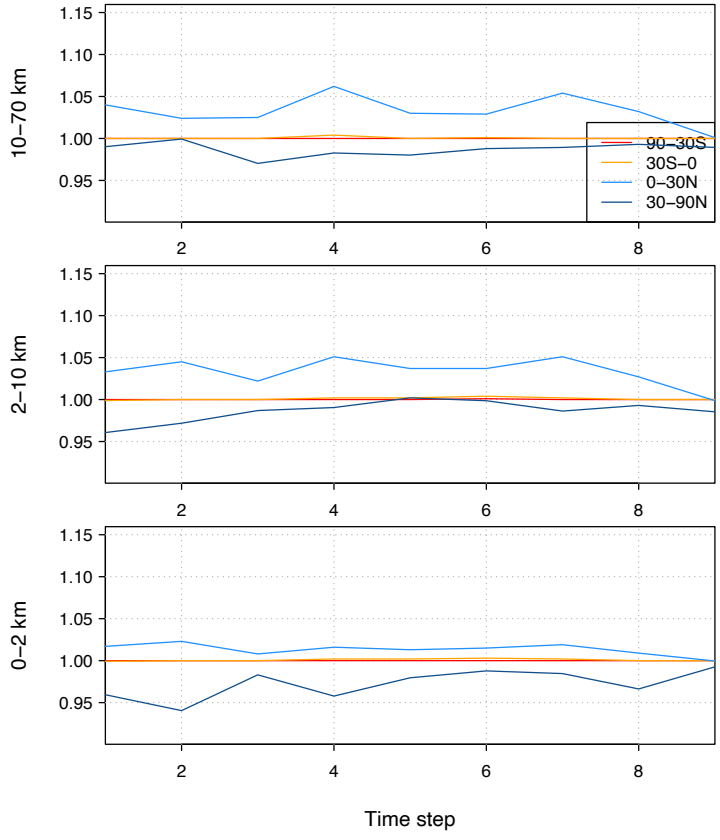

https://doi.org/10.5194/egusphere-2025-147
Preprint. Discussion started: 25 February 2025

Figure 4: Area-weighted mean XCH_4 for two-weekly intervals integrated over the domain for the inversion using EGG4 for the boundary conditions.

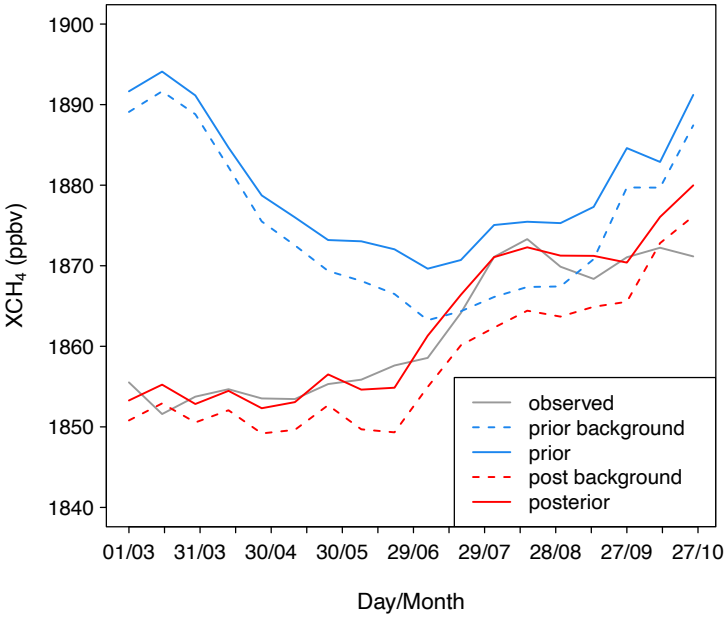

https://doi.org/10.5194/egusphere-2025-147
Preprint. Discussion started: 25 February 2025

Figure 5: Mean flux of CH_4 (units of g/m^2/day) from the inversion using TROPOMI a) prior, b) posterior and c) the flux increments.

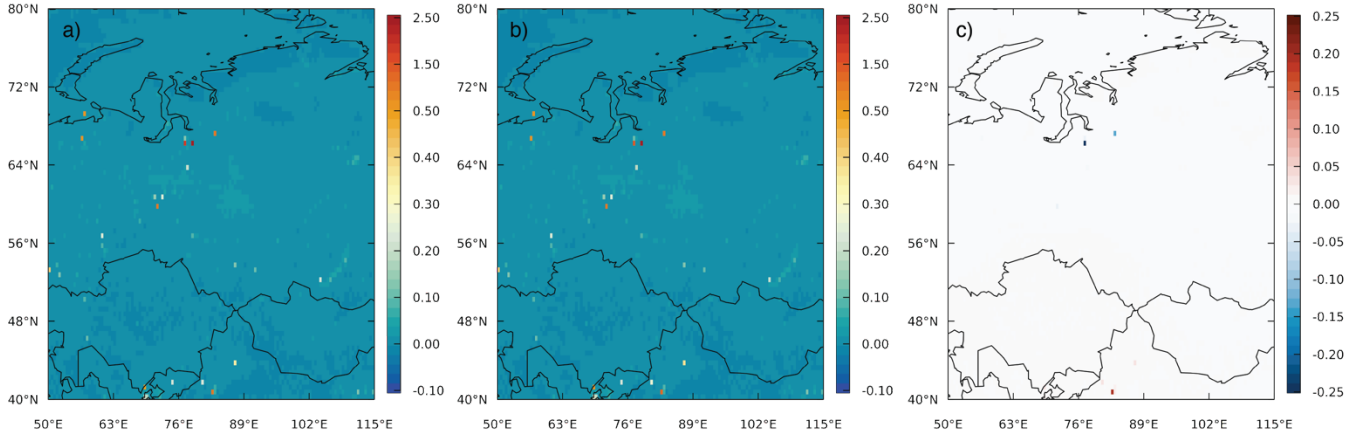

520

https://doi.org/10.5194/egusphere-2025-147
Preprint. Discussion started: 25 February 2025

Figure 6: Total CH_4 source for the domain shown 2-weekly for the prior estimate and for the posterior estimates from the TROPOMI and ground-based observation inversions.

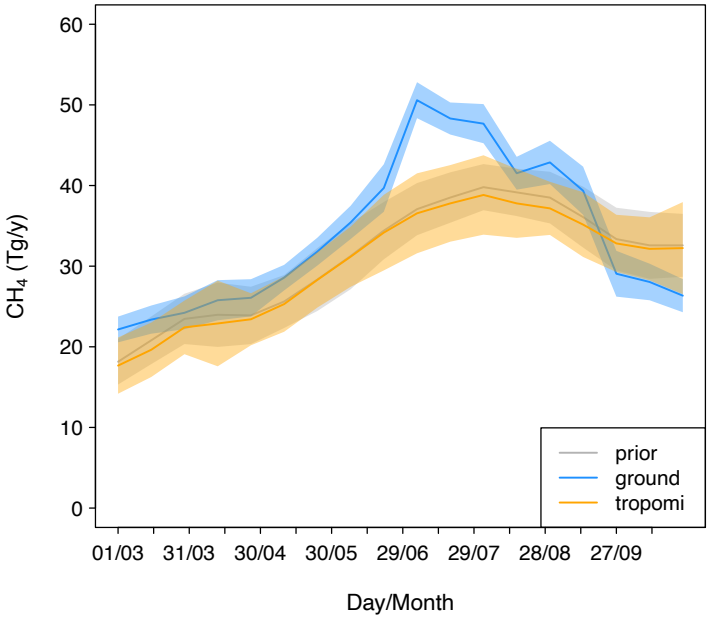

525

https://doi.org/10.5194/egusphere-2025-147
Preprint. Discussion started: 25 February 2025

Figure 7: Uncertainty reduction for the inversion using TROPOMI a) mean of March to October, b) mean March to May, c) mean June to August

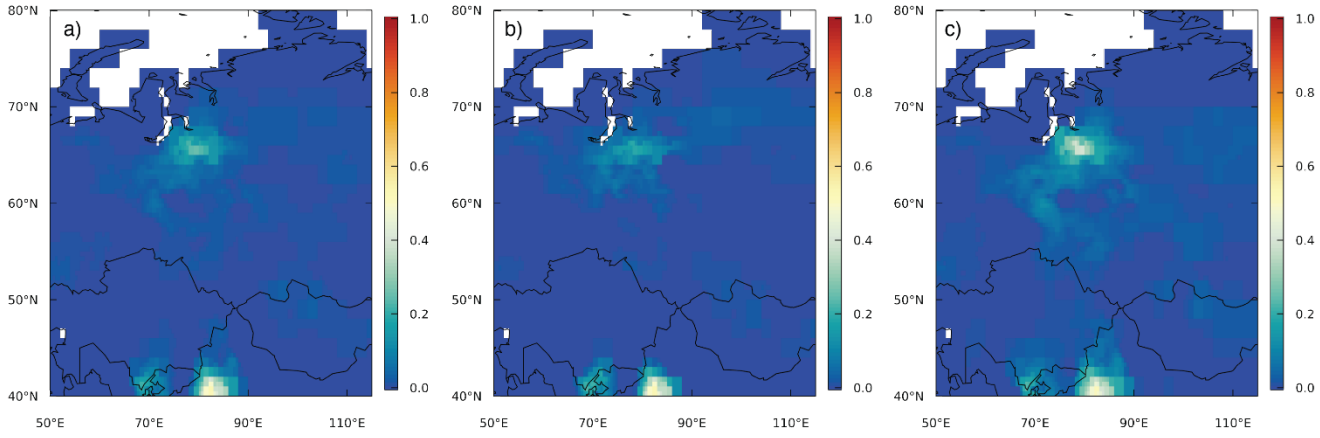

530

https://doi.org/10.5194/egusphere-2025-147
Preprint. Discussion started: 25 February 2025

Figure 8: Mean flux of CH_4 (units of g/m^2/day) from the inversion using ground-based observations, a) posterior, b) flux increments, and c) difference with respect to the posterior fluxes from the inversion using TROPOMI observations.

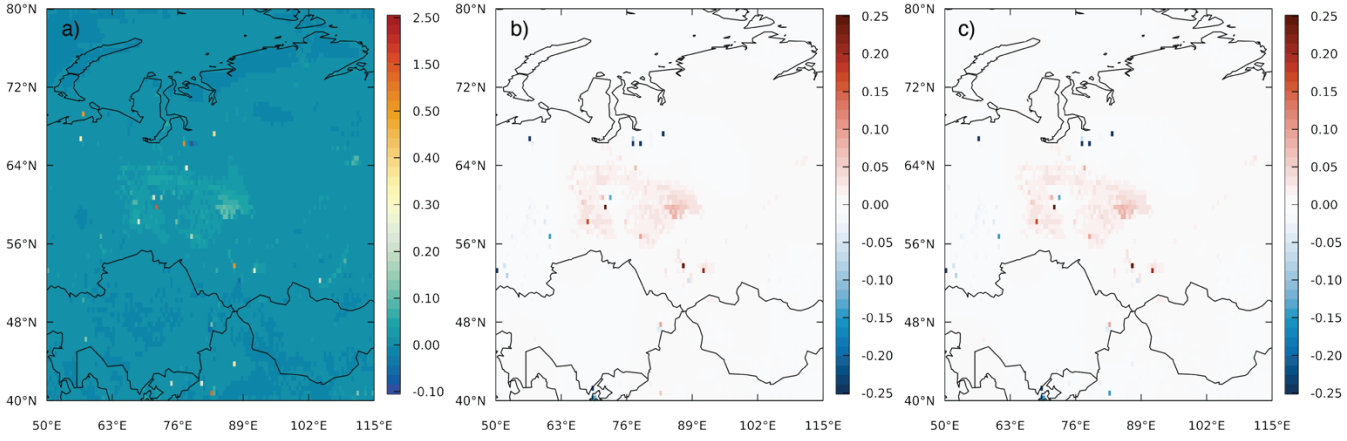

https://doi.org/10.5194/egusphere-2025-147
Preprint. Discussion started: 25 February 2025

Figure 9: Uncertainty reduction for the inversion using ground-based observations. The observation sites are indicated by the yellow circles.

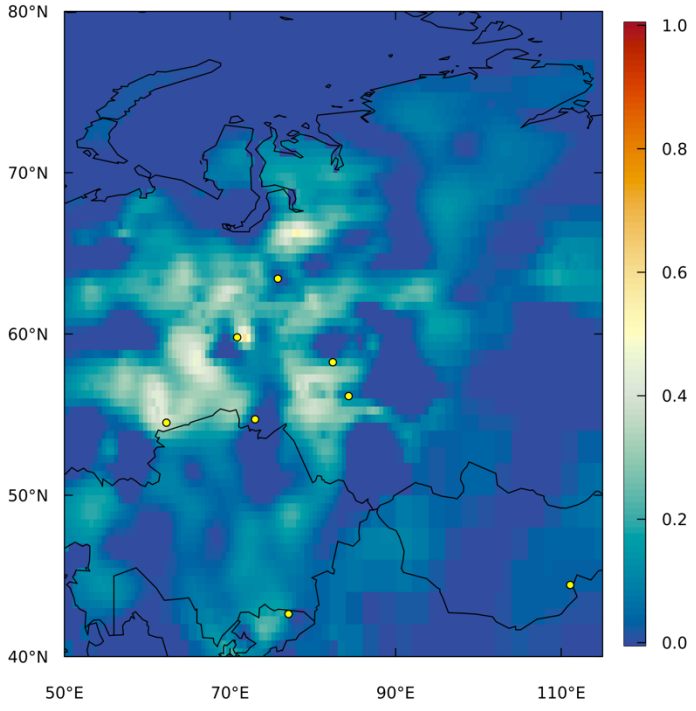

https://doi.org/10.5194/egusphere-2025-147
Preprint. Discussion started: 25 February 2025

Figure 10: Taylor diagram for the comparison of modelled versus observed CH_4 mixing ratios at ground-based sites. The angle gives the Pearson's correlation and the x-axis gives the normalized standard deviation for the comparison. Each point represents a site and the colour of the point indicates the modelled data used (prior: using the prior fluxes, ground: using the posterior fluxes from the inversion with ground-based observations, tropomi: using posterior fluxes from the inversion with TROPOMI observations). All model simulations used optimized boundary conditions to compare differences solely due to the fluxes used.